Available online at www.sciencedirect.com

ScienceDirect

journal homepage: www.elsevier.com/locate/he

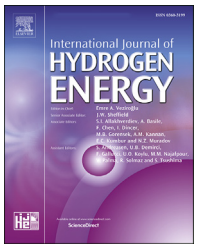

Modelling and optimization of a flexible hydrogen-fueled pressurized PEMFC power plant for grid balancing purposes

Elena Crespi [a,*], *Giulio Guandalini* [a], *Sönke Gößling* [b], *Stefano Campanari* [a]

[a] *Group of Energy Conversion Systems, Department of Energy, Politecnico di Milano, Via Lambruschini 4A, Milan, 20156, Italy*

[b] *ZBT, Carl-Benz-Str. 201, 47057, Duisburg, Germany*

HIGHLIGHTS

- Comparison of two innovative layouts of MW-scale flexible PEM FC power plant.
- Stack performance based on experimental data.
- System pressurization improves the FC stack gross efficiency.
- The adoption of an air expander improves the system net efficiency.
- An optimal pressurization strategy can be defined as function of load.

ARTICLE INFO

Article history:
Received 1 December 2020
Received in revised form
9 January 2021
Accepted 12 January 2021
Available online 25 February 2021

Keywords:
PEM fuel cell
Flexibility
MW-scale plant
Grid balancing
Pressurized fuel cell

ABSTRACT

In a scenario characterized by an increasing penetration of non-dispatchable renewable energy sources and the need of fast-ramping grid-balancing power plants, the EU project GRASSHOPPER aims to setup and demonstrate a highly flexible PEMFC Power Plant, hydrogen fueled and scalable to MW-size, designed to provide grid support.

In this work, different layouts proposed for the innovative MW-scale plant are simulated to optimize design and off-design operation. The simulation model details the main BoP components performances and includes a customized PEMFC model, validated through dedicated experiments.

The system may operate at atmospheric or mild pressurized conditions: pressurization to 0.7 bar_g allows significantly higher net system efficiency, despite the increasing BoP consumptions. The additional energy recovery from the cathode exhaust with an expander gives higher net power and net efficiency, adding up to $2\%_{pt}$ and reaching values between $47\%_{LHV}$ and $55\%_{LHV}$ for currents between 100% and 20% of the nominal value.

* *Corresponding author.*
E-mail address: elena.crespi@polimi.it (E. Crespi).

https://doi.org/10.1016/j.ijhydene.2021.01.085

Introduction

Renewable energy is at the core of Energy Union's priorities. Very ambitious targets on the share of total energy consumptions coming from RES are specified in the European directives on the promotion of use of energy from renewable sources [1,2] including a binding renewable energy target for the EU for 2030 of 32%.

To reach these targets, a key contribution is given by increasing the share of electricity production from RES. However, the increasing penetration of non-programmable RES may hinder the security and reliability of the transmission and the distribution grids, being their generation mainly uncertain and dispersed.

Many studies have investigated the effects that a high penetration of RES have in term of backup generation and storage needs [3–7]; analysing options for grid improvement [8] and comparing introduction of storage systems as well as grid extension and repowering [9]. The concept of Smart Grid [10–12] is considered at international level, taking advantage of the increased intelligence and flexibility of the grid to facilitate the connection of Dispersed Generation (DG) units, increase the reliability and security of supply and allow the consumers to contribute in optimizing the operation of the system with Demand Response schemes. Indeed, the use of distributed generation resources (Transmission Integrated Grid Energy Resource) has already emerged as an opportunity to enhance grid characteristics, reducing line losses and providing local voltage support in regions with poor load/generation balance [13]. Furthermore, moving away from the fit and forget approach of connecting DG to electric power systems to a policy of integrating DG into power system planning and operation through active management of distribution networks allows to overcome the key issues concerning the integration into the electric power system of DG, allowing them also to provide ancillary services [14].

It is therefore necessary to evolve the system to more efficient networks. To be able to follow the sudden changes in generation, it is necessary that enough flexible resources are available and that the system planners have access to new tools to understand the volatility in the net load and to map that to a flexibility requirement [15]. In this framework, the Clean Energy for All European package [2] has introduced new electricity market design rules in order to help the energy markets to include more renewables, empower consumers, and better manage energy flows across the EU. With these new energy market rules, prosumers (i.e. both producers and consumers) are put at the heart of the transition: they are enabled to participate actively in the energy market with Demand Response schemes and infrastructures, varying its consumptions and/or production in response to price changes to profit from the optimal price conditions, contributing to grid efficiency and integration of RES.

Among all the sources of flexibility, MW-scale stationary Fuel Cell Power Plant (FCPPs) based on low temperature Proton Exchange Membrane Fuel Cells (PEMFC) are seen as flexibility enablers for prosumers through the use of hydrogen, a source for clean and CO_2-free dispatchable and distributed electricity generation [16]. PEMFC system have indeed very fast ramp rates and excellent load following capabilities that make them perfectly suited for grid balancing and participation to the Ancillary Service market [17–21], resulting an essential technology for the future renewable based energy infrastructure.

In this framework, the GRASSHOPPER (GRid ASsiSting modular HydrOgen Pem PowER plant) FCH-JU2 European Project [22] aims to realize a next-generation MW-size PEM FCPP, which is cost-effective and flexible in power output, specifically designed for the provision of ancillary services to the power grid.

Background and paper novelty

GRASSHOPPER project sets up and demonstrates an innovative 100 kW_{el} PEM FCPP unit, scalable to the MW size, aiming at analysing how distributed and fast-ramping fuel cell systems can be used to provide grid support with a Demand Side Management program. The project leverages previous experiences from the previous European Project DEMCOPEM-2MW [23,24] and aims at a substantial design re-optimization, coherently improving MEA, stack and system together, to achieve improved cost targets. In parallel to the development of new stacks with improved performance, an important role is played by the reduction of the cost of the FCPP balance of plant components and the improvement of their dynamic behavior. The optimal integration of components and the definition of the plant layout is supported by modelling activities that allow to simulate the stationary behavior of the plant both at nominal point and at partial load operation, analyzing the effects that different operating parameters (e.g. backpressure, air stoichiometry, etc.) have on both gross FC efficiency and net plant efficiency. Results obtained through the modelling activities support future plant scale-up to MW-scale, improving plant configuration and identifying the optimal operating parameters for further developments.

Many studies in literature analysed PEMFC systems designed for residential combined heat and power (CHP) production. As an example, the optimal operating conditions for a 1-kW PEMFC-based CHP system coupled with an apartment house are determined in Ref. [25], while in Ref. [26] the dynamic performance and transient response of a commercial 1.2 kW PEMFC system are analysed. The system includes the hydrogen supply system, an air compressor, a moisture exchanger for air humidification and an air-based cooling system. Results shows overshoot and undershoot behaviors during transients. In Ref. [27], a pilot PEM Power Plant with a 70 kW_{el} fuel cell unit and utilizing by-product hydrogen from the electrolysis of brine is described, reporting performance for a period of five and a half years, showing cell reversible and irreversible decay over 30,000 h of operation. In Ref. [28], it is reported that a 50 kW_{el} PEMFC pilot plant has been operated 4400 h using hydrogen originating from a sodium chlorate production process after standard industry purification, where the relatively low quality of hydrogen did not lead to extensive cell degradation. The scale-up to a $2MW_{el}$ FCPP based on PEMFC, working in stationary conditions in industrially relevant environment using hydrogen from a chlor-alkali process, has been demonstrated in Ref. [23].

Nevertheless, the studies about PEMFC systems in the scientific literature are focused on their performance at nominal or constant load, on the evaluation of voltage decay issues, or deal with optimization for the fuel cell integration in CHP systems. Their performance at partial load and in dynamic load-following conditions are usually not described.

The flexibility potential of PEMFC systems is instead exploited for mobility application, in naval and mostly in automotive systems. The use of a PEM fuel cell system for maritime application is investigated in detail in Ref. [29], analyzing the best operative strategy in terms of energy efficiency, CO_2 emissions and costs, in comparison with the state-of-the-art solution for ships (fuel oil internal combustion engines). A PEM fuel-cell-battery hybrid system, including two parallel 28 kW PEM FC modules for the propulsion of a 20 m long tourist boat is developed and demonstrated in Ref. [30]. The issue related to the energy management strategy in vehicles with hybrid power system is investigated in Ref. [31], proposing a battery-based solution to reduce fuel consumption and power fluctuations. Differently from FC system for stationary application which are generally working at atmospheric pressure, FCs for automotive application usually operate at 2–2.5 bar, typically using electric compressors but also compressor-turbine arrangements [32]; as an example, in Ref. [33] a preliminary design method for an on-board turbine to recover energy from the exhaust stream is proposed. In other cases, pressurization arrangements have been studied for aeronautical applications [34].

Many studies have also focused on the development of detailed models of the cells. A lumped model of a single cell is developed and validated in Ref. [35] and a general PEM fuel cell model able to predict steady-state cell behavior, including membrane aging, is described in Ref. [36]. A parametric study of PEMFC performance, analyzing different operating temperatures, cathode and anode humidification levels, and operating pressures has been carried out in Ref. [37]. Other studies focus on reproducing a single phenomenon, such as oxygen mass transfer in the diffusion layer [38] or water vapour diffusion in the diffusion layer [39], or the effect of different cooling methods [40].

On the contrary, detailed stationary models of PEM FC systems, including BoP components, are not easily found in literature, especially for multi-kW or MW scale systems. As an example, in Ref. [41], a zero-dimensional model of a 3 kW_{el} PEMFC cogenerative system for residential application has been developed in Aspen Plus environment, to assess the system performance varying the operating condition (temperature, pressure and relative humidity). However, the model includes only the FC stack and the heat exchangers for heat management, while details on the other BoP components are not provided.

System models are instead developed for automotive systems, where control issues arise. In Ref. [42], a control-oriented model of a PEM FC system for automotive application is developed to investigate the system transient response. In Ref. [43] a dynamic plant simulation model of a 75 kW FC system incorporating the BoP components is developed and used to improve the air supply subsystem, while in Ref. [44] a dynamic model of a hybrid FC-battery system for application in a vehicle is presented. However, the architecture of FC systems for automotive applications has peculiarities, mainly due to the limited space and weight issues. The FC stationary power plant can exploit alternative technologies, maintaining the dynamic and partial load performance of automotive systems. Hence, the characteristics of MW-scale stationary systems cannot be directly deducted from automotive FC systems.

In this study, a stationary MW-scale PEM FCPP newly designed for highly dynamic application (grid balancing) is modelled and simulated. The model includes all the main balance of plant components and their part-load operation. The work presents a novel solution for the stationary FC system layout and its operative strategy. Some of the features of automotive systems are adapted to stationary layout and it is proposed the possibility of pressurizing the system and recovering also energy from the stack cathode exhausts. The characterization of the fuel cell performance exploits semi-empirical polarization curves, where the model parameters are derived from experimental data acquisition on state-of-the-art PEM cells, previously unpublished and presented in detail in this work. The cell model includes the voltage dependence on cell temperature, cathode backpressure, air relative humidity and stoichiometry (see section 'Polarization curves'). These parameters are of great importance for system optimization, which can differ strongly from single cell optimal operating conditions; indeed the cell model is integrated in the complete system and used for linked cell-system optimization. Additionally, given the final purpose of grid services provision, the model is used to analyze the plant behavior over the entire range of operation (from minimum to maximum load), obtaining a complete operation map of the system.

A detailed description of the innovative MW-scale plant simulation model, based on the 100 kW_{el} pilot plant layout developed in the GRASSHOPPER project, is given in Section 'PEMFC system layout'. A detailed description of the modelling approach is then provided in Section 'Modelling approach' and the results of the system simulations are reported in Section 'Complete plant simulations results'. Since the fuel cell performance is expected to increase at higher pressure (thanks to a higher cell voltage) [45], simulations are performed to study the behavior of the FC power plant when operated at different pressures, from ambient to mildly pressurized conditions (0.7 bar_g). Two different system layouts are considered, mainly differing for the presence of an air expander for energy recovery, assessing the effects of pressurization on the performance of the entire system. The main conclusions are synthetized in Section 'Conclusions'.

PEMFC system layout

The plant layout simulated in this work has been proposed as a possible scale up of the flexible pilot plant developed in the GRASSHOPPER H2020 project. The main components arrangement is shown in Fig. 1. The modular PEM Fuel Cell includes several identical stacks, supplied with pure hydrogen and air. In order to enhance performance and durability of the cells, reactants humidity and pressure as well as cells temperature have to be controlled. In this respect, dedicated

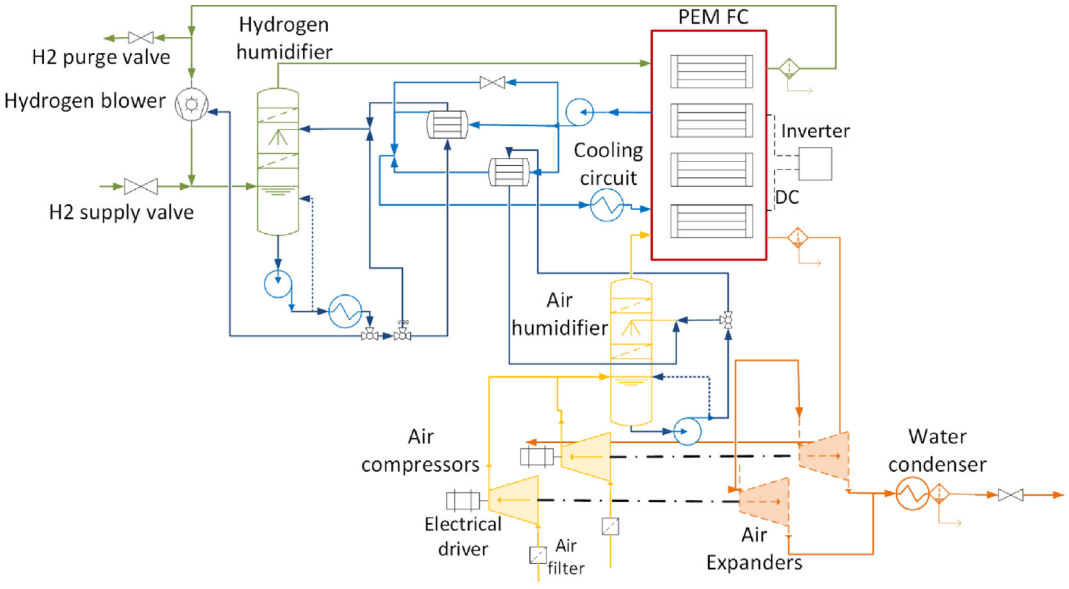

Fig. 1 – Simulated MW-scale FC plant configuration.

reactants humidifiers and a cooling circuit using water-glycol mixture have been included.

Pure hydrogen is assumed available at plant inlet at a sufficiently high pressure (above a minimum of 2 bar), avoiding a compression step. This assumption is reasonable since hydrogen comes from upstream processes or from a buffer tank that operates above atmospheric pressure. The exhaust hydrogen from the anode outlet is recirculated to increase the total hydrogen utilization factor by means of a compressor. A purge valve on the hydrogen line avoids inert gases build-up, while fresh pure hydrogen enters the system in the humidifier.

Fresh air is compressed, humidified and fed to the FC stacks cathode. The flexibility target of the plant requires multiple compression units properly arranged in order to grant the appropriate operating conditions in the full load range of the FC. The compressor configuration selection is discussed in section 'Air compression unit layout selection'.

Both air and hydrogen humidification are performed in a shower-type packed-bed humidifier to take advantage of its scrubbing effect. A small amount of water is continuously recirculated internally to the humidifier to be filtered, while a purge removes the water produced in the FC avoiding build-up. A network of heat exchangers and bypass pipes allows to transfer heat from the cooling circuit to both humidifiers, controlling accurately the temperature and consequently the relative humidity of the reactants at the cell inlet. Finally, the temperature of the coolant at FC stacks inlet is controlled in a dedicated heat exchanger, using a separate external cooling circuit. The coolant pump is regulated to vary the coolant flow rate maintaining the design stacks temperature at any load.

The exhaust-air line can be designed according to two different options:

- air exiting the FC cathode is cooled to condensate the water vapour and separate the demineralized water. Air is then released into the atmosphere, flowing through a back-pressure valve that controls the FC pressure.
- air exiting the FC cathode is first expanded in order to recover useful energy. In this case, the expanders directly provide mechanical power to the compressors; both the machines adopt a similar volumetric technology and are ideally placed on the same shafts. Air cooling, water recovery and release into the atmosphere are then performed as in the first option. Other options for the coupling of the expander with the compression unit (e.g. electrical coupling) are also possible, but not considered here.

Modelling approach

The plant has been modelled using the process simulation tool Aspen Plus® [46], a commercial simulation code for energy and chemical plants design and rating.

Standard components are available for all the main plant units, with the exception of the PEM FC stacks, for which a customized model in the Aspen Custom Modeler language has been implemented.

The modelling activity aims at simulating both the proposed layout options, mainly differing for the presence of the air expander. For both options, the performances of the FCPP while working in different operating points are analysed and compared. The plant operating conditions are optimized, investigating the effects of adopting different control strategies both in nominal and off-design conditions.

PEMFC stack model

As mentioned above, a custom model is realized for the PEM FC, using the Aspen Custom Modeler® language and considering a lumped-volume approach. Indeed, given the size of the problem where thousands of cells are present, a detailed

description of the internal geometry of a single cell would increase the computational cost without being necessary to reproduce large scale effects, which are the object of this work. The 0D model is actually able to calculate the produced power on the base of regressed polarization curves and to solve mass and energy balances on the stacks to determine outlet gas flows composition and temperature, allowing to evaluate the cells performance in different operating conditions. Outlet gas pressure is also computed considering the dependence of pressure drops in the channels on the volumetric gas flow rates.

Since the FC model has a modular structure, the lumped model of a single cell is realized, solving mass and energy balances and calculating the performance through semi-empirical polarization curves. Then, the FC stacks are built connecting several identical cells electrically in series. Finally, the stacks are in turn electrically connected in parallel and/or in series to reach the desired FC size. In this work, it is assumed a reference size of 1 MW of gross DC power generation at the nominal cells operating conditions, as defined for Grasshopper H2020 project [22] and reported in Table 1. Details on the number of stacks and on the number of cells per stacks are here omitted for confidentiality.

Throughout the paper we will often use the concept of fuel excess and air excess with respect to the stoichiometric values. The ratio of the air flow rate with respect to the stoichiometric flow rate is labelled 'air ratio to stoichiometry' or simply 'air stoichiometry'. Similarly, the ratio of the fuel flow rate with respect to the stoichiometric flow rate is labelled 'fuel ratio to stoichiometry' or simply 'fuel stoichiometry'.

The semi-empirical current-voltage polarization curves aim at reproducing the real cells performances. They are obtained from simplification of the theoretical polarization curve equation, regressing the coefficients on the basis of a dataset obtained from experimental measurements on test cells. Details are provided in section 'Polarization curves'.

Polarization curves

In order to calibrate the fuel cell model parameters, a measurement data set of the specific fuel cell is necessary. Conversely, the simulation aims at designing the optimal operating conditions for the fuel cell and the matching fuel cell system, and since the fuel cell is not yet fully developed, no specific measurement data are available. However, in the process of designing the fuel cell, smaller test cells have been manufactured and are used at ZBT with materials and specifications similar to the final ones, which enable early extrapolation of the fuel cell performance by means of various methods.

The design of the Grasshopper H2020 stack will be based on the "FFF-design" flow field of ZBT and the dimensions of the channel and landing widths will be based on it. The "FFF-design" flow field is designed to enable using the test cell "quickCONNECT fixture" from balticFuelCells GmbH (a test cell system for characterization of fuel cells with adjustable contact pressure [47], in the version with 25 cm^2 active area, to operate at stoichiometries in a range from 1.5 to 5. The design uses channel and landing widths in the range of 0.4 mm. The test cell is integrated in a test rig where the cathode and anode reactants are conditioned to defined dew points by means of a bubble humidifier. After the bubble humidifiers, the media are fed to the cell via temperature-controlled pipes and tubes. The outflowing media of the test cell are cooled, the liquid water is separated and then the inlet pressure is adjusted by using a pressure regulator. In order to condition the MEA, the cell is operated several times in a cycle with loads in the high, medium and low voltage range; the cycle includes hydrogen starvation phases and provides a cooling down to 30 °C. After the experimental determination of each polarization curve, the cell is cooled for 30 min without load.

For the individual polarization curves, the MEA is conditioned at 0.6 V for 60 min, with the specific operating conditions to be investigated, and then the maximum current density of 2.5 A/cm^2 is approached. While this maximum operating point is maintained for 30 min, the other current densities are kept for only 20 min each. The last minute of each operating point is used for further analysis.

The available dataset (Table 2) allows to evidence the effects on the voltage of three operating parameters: stack backpressure, air stoichiometry and relative humidity of the supplied air. The influence of the hydrogen stoichiometry is not shown, because this parameter is kept constant in all tests, therefore its effect is not included in the model; it is however known from previous experiences that its influence on cells performances is low [23]. In the entire dataset, the supplied hydrogen relative humidity is kept constant at 50% based on the cell temperature. All curves are available for current densities between 0 and 2.5 A/cm^2 and operating temperature of 65 °C. The polarization curves are shown in Fig. 2.

Comparison among curves characterized by the same pressure at FC stacks outlet and different air ratios to stoichiometry allows to study the effect of the air flow rate on the cell voltage (Fig. 2b and d). The comparison among curves Pol 1 and Pol 6 (Fig. 2d), both obtained in mildly pressurized conditions (backpressure 0.6 bar_g) but with different air stoichiometry, shows that an increase of the air stoichiometry from 2

Table 1 – Stack nominal operating conditions [22].

Nominal FC operating conditions	
Current density	1.0 A/cm^2
Air stoichiometry	2.0
Hydrogen stoichiometry	1.5
Air/Hydrogen averages RH	100%
Air backpressure (stack outlet)	0.1–0.7 bar_g bar_g bar_g
Hydrogen backpressure (stack outlet)	0.1–0.7 bar_g
Stack temperature	70 °C
Coolant temperature gain	10 °C

Table 2 – Polarization curves dataset characterization.

	p [bar_g]	Air RH [%]	Air stoich.	H_2 RH [%]	H_2 stoich.
Pol 1	0.6	50%	2	50%	1.25
Pol 2	0.35	50%	2	50%	1.25
Pol 3	0.1	50%	2	50%	1.25
Pol 4	0.1	50%	3	50%	1.25
Pol 5	0.1	75%	3	50%	1.25
Pol 6	0.6	50%	3	50%	1.25
Pol 7	0.6	75%	2	50%	1.25
Pol 8	0.6	40%	2	50%	1.25

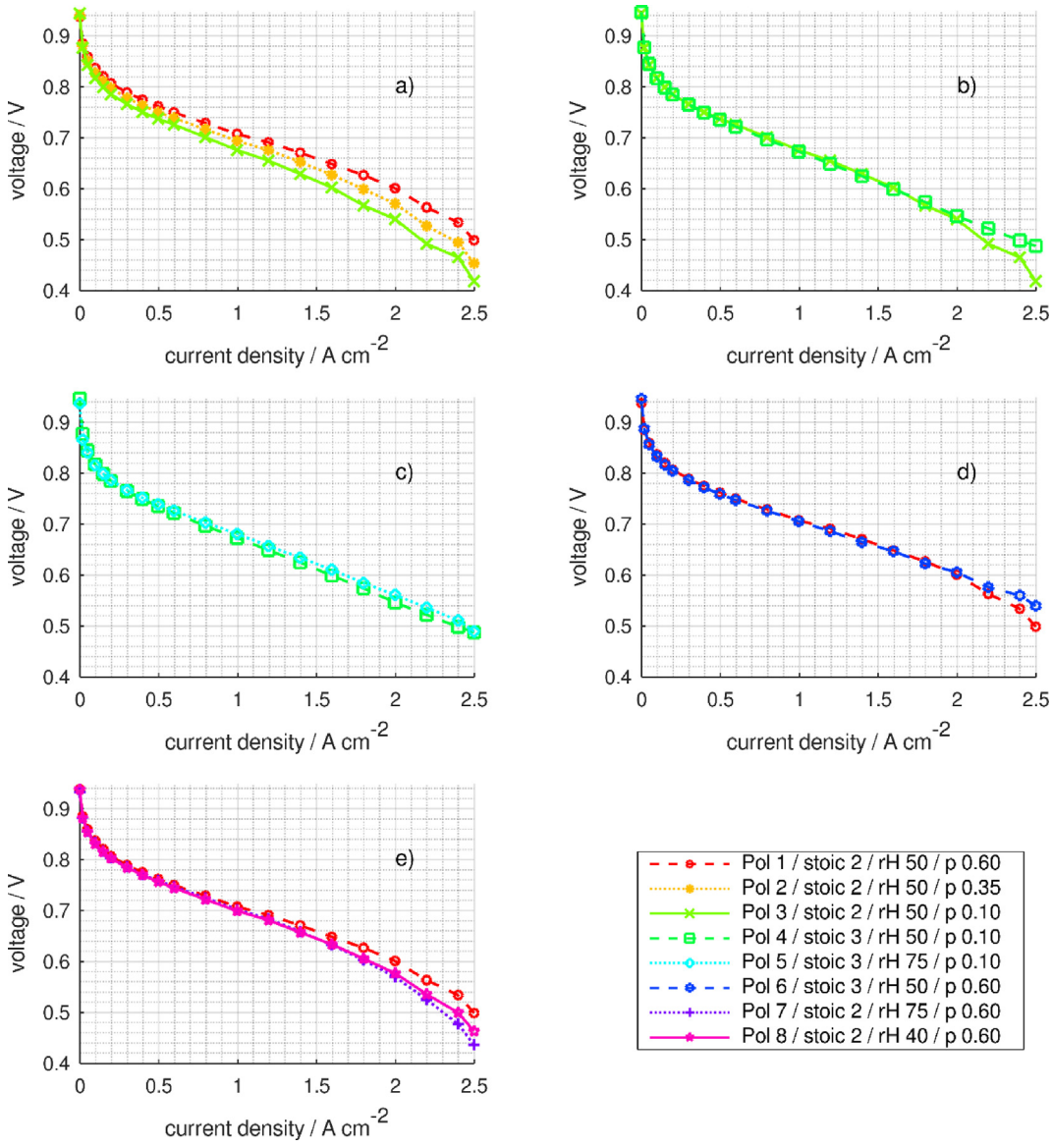

Fig. 2 – Experimental data. Every plot is showing a single parameter variation, polarization curve 1 (Pol 1) represents the reference. Plot a) shows the influence of the operating pressure, plot b) the influence of the air stoichiometry at a pressure of 0.1 bar_g, plot c) the influence of an increased cathode humidity at 0.1 bar_g, plot d) the influence of air stoichiometry at 0.6 bar_g and plot e) the influence of inlet air humidity at 0.6 bar_g.

to 3 leads, while working at nominal current (1 A/cm^2), to a voltage gain equal to 1.8% of the voltage. The voltage gain increases further with the current density, reaching about 2.9% at 1.5 A/cm^2. On the contrary, by comparing curves Pol 3 and Pol 4 (Fig. 2b), both obtained with backpressure 0.1 bar_g and with air stoichiometry equal to 2 and 3 respectively, the voltage gain due to an increase in the air stoichiometry turns out to be negligible (0.3% at 1 A/cm^2).

Furthermore, comparison among curves characterized by the same air stoichiometry and different pressure levels allows to analyze the effects of pressurization on the cell voltage (Fig. 2a). Comparison among the curves Pol 1 (mildly pressurized - backpressure 0.6 bar_g) and Pol 3 (not pressurized – backpressure 0.1 bar_g), both obtained with an air stoichiometry equal to 2, shows that operation at nominal current (1 A/cm^2) with a mild pressurization allows a small voltage gain, nearly 2.5% of the voltage. The typical impact of the pressurization on the kinetic region can be seen. This voltage gain increases with the current density, reaching 3.5% of the voltage value at 1.5 A/cm^2. The positive effect on the voltage is noted also by comparing Pol 4 and Pol 6, obtained both with air stoichiometry equal to 3 and with backpressure equal to 0.1 bar_g and 0.6 bar_g respectively. In this case, the voltage gain is equal to 4.6% of the voltage value at nominal current and to 6.9% at 1.5 A/cm^2.

The influence of cathode humidity must be considered in a differentiated way. In Fig. 2c, a positive effect can be illustrated by increasing the humidity. The low pressure here means that the air does not saturate so quickly through the product water and increased humidity at the inlet still has a

very positive effect. At a pressure of 0.6 bar g (Fig. 2e), on the other hand, the humidification of the reference curve (Pol 1) already represents an almost optimal condition. Both an increase (Pol 7) and a reduction (Pol 8) in humidity lead to reduced cell voltages, which can be caused by blocked diffusion paths (Pol 7) and reduced membrane conductivity (Pol 8).

Simplified polarization curve model

The polarization curves obtained by means of the experimental cell tests are then included in the PEMFC model, aiming at reproducing the performance of the real cells when included in the complete system. The adopted polarization curve formulation is shown in Eq. (1), where V_{cell} [V] is the cell voltage and $i\,[mA/cm^2]$ is the cell current density. The first term represents an apparent open circuit voltage, the second term the ohmic losses, the third and the last terms represent the activation and the concentration overvoltage respectively. The structure of the equation is similar to the conventional equations in literature [48], but it has been modified to make explicit the influence of pressure and air stoichiometry according to the experimental data evidences. Hydrogen concentration influence has been neglected according to preliminary experimental data.

$$V_{cell} = V_{OC} + \frac{R_{ohm,1}}{\left(\frac{x_{H_2O}}{x_{H_2O,ref}}\right)^{G_{ohm}}} \cdot i + \left(K_{act,1} + K_{act,2}\left(\frac{p}{p_{ref}}\right)^{\frac{x_{O_2}}{x_{O_2,ref}}}\right) \cdot ln\left(1+\frac{i}{i_0}\right) + \left(K_{conc} \cdot \left(\frac{p}{p_{ref}} \cdot \frac{x_{H_2O}}{x_{H_2O,ref}}\right)^{G_{conc}}\right) \cdot ln\left(1-\frac{i}{i_L \cdot \frac{p}{p_{ref}}}\right) \quad (1)$$

In this formulation, the effect of the air stoichiometry is included considering the dependence of the activation overvoltage on the oxygen concentration. The oxygen concentration (x_{O_2}) is evaluated as an average between inlet ($x_{O_2,in}$) and outlet oxygen molar fraction ($x_{O_2,out}$). The use of the average value makes the solution implicit but allows for including the effect of utilization factor and water production. This value is then made non-dimensional dividing by the oxygen molar fraction reference value ($x_{O_2,ref}$), computed in the case of stoichiometric reaction ($x_{O_2,out} = 0$):

$$\frac{x_{O_2}}{x_{O_2,ref}} = \frac{x_{O_2,in} + x_{O_2,out}}{x_{O_2,in}} \quad (2)$$

$$x_{O_2,in} = x_{O_2,air}\left(1 - RH_{a,in} \cdot x_{sat}\right) \quad (3)$$

where $RH_{a,in}$ is the relative humidity of the intake air and x_{sat} is the water molar fraction for air in saturated conditions, evaluated at the average stack temperature.

$$x_{O_2 out} = \frac{x_{O_2,in}\left(1 - \frac{1}{S_a}\right)}{1 + \frac{x_{O_2,in}}{S_a}} \quad (4)$$

where S_a is the air stoichiometry, defined as the ratio between the air flow rate entering the stack and the one required to have stoichiometric reactants.

This expression for $x_{O_2,out}$ is obtained by a mass balance, considering the whole amount of water at the cathode outlet, i.e. inlet water flow plus produced water.

The voltage dependence on the air relative humidity is introduced in the ohmic losses and in the concentration overvoltage. The cathode water content is computed as average between water molar fraction at cathode inlet ($x_{H_2O,in}$) and at cathode outlet ($x_{H_2O,out}$). This value is then normalized vs. its reference value ($x_{H2O,ref}$, see Eq. (5)), set equal to the molar water fraction in saturated conditions, for which the best cell performances are expected.

$$\frac{x_{H2O}}{x_{H2O,ref}} = \frac{x_{H_2O,in} + x_{H_2O,out}}{2\,x_{H_2O,ref}} \quad (5)$$

$$x_{H_2O,in} = RH_{a,in} \cdot x_{sat} \quad (6)$$

$$x_{H_2O,out} = \frac{x_{H2O,in} \cdot S_a + 2 \cdot x_{O_2,in}}{S_a + x_{O_2,in}} \quad (7)$$

The voltage dependence on the fuel relative humidity is instead neglected, since no experimental data are available to investigate the voltage dependence on the anode water content (the anode relative humidity is kept constant at its nominal value during stacks operation); however, the corresponding effect could be included using a similar formulation.

The effect of the backpressure (p) is directly included in the activation and concentration overvoltage, and indirectly included in the terms containing the molar water fraction in saturated conditions. The reference pressure (p_{ref}) is assumed equal to ambient pressure.

The numerical values of the coefficients appearing in Eq. (1), obtained from the experimental data regression, are reported in Table 3. The parameters are regressed to minimize the error between model and polarization curves data, focusing on the range of current density where the cell will generally operate (200–1000 mA/cm^2).

Fig. 3 shows that the proposed equation fits with a good approximation the experimental data for different backpressures and air stoichiometry (at fixed air relative humidity – 50%) and for different air relative humidity (at fixed air backpressure – 0.6 bar$_g$ – and air stoichiometry – 2). The random distribution of the residuals (Fig. 4) shows that the chosen formulation catches the general behavior of the data.

Table 3 – Polarization curve coefficients regressed on experimental data.

Coefficient	Regressed value	
V_{OC}	928.24	mV
R_{ohm}	−0.045	$\Omega \cdot cm^2$
G_{ohm}	0.837	-
$K_{act,1}$	−41.06	mV
$K_{act,2}$	5.62	mV
i_0	4.86	mA/cm^2
K_{conc}	126.50	mV
i_L	2600	mA/cm^2
G_{conc}	1.183	–

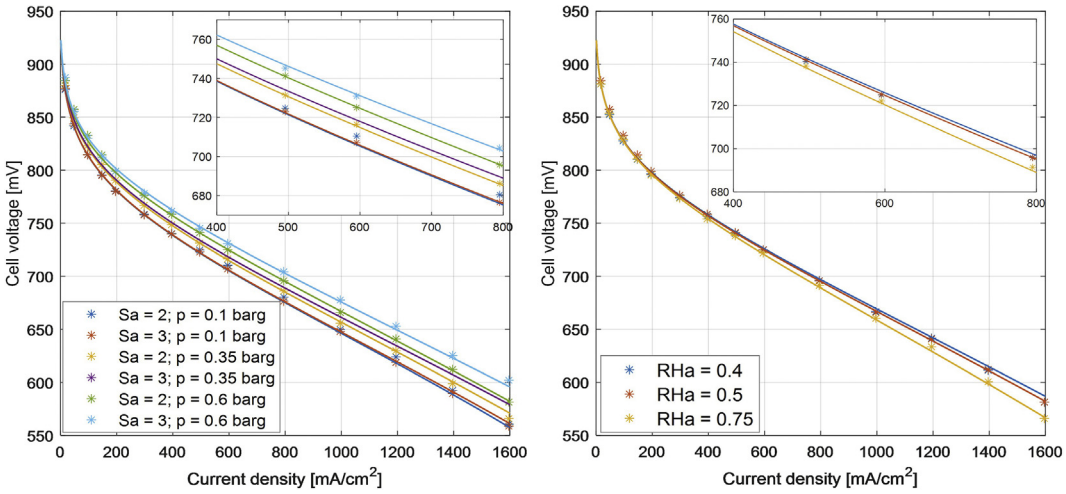

Fig. 3 – Comparison between experimental dataset and regressed polarization curves for different FC stack backpressure and air stoichiometry (left) and different inlet air relative humidity (right).

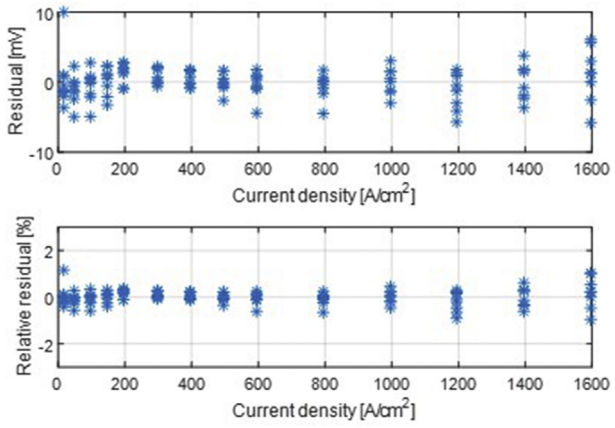

Fig. 4 – Plot of residuals Vs current density.

Relative errors are always below 1% for relevant currents values (200–1500 mA/cm^2).

Stacks pressure drops

The pressure drops of the fluid in the channels of the cells are calculated as a function of the flow rate. Since velocities in the flow field are low, the flow regime is laminar and the following formulation for the pressure drops (expressed in bar) can be considered:

$$\Delta p = \lambda\rho\frac{L}{D}\frac{v^2}{2} + \sum K_f\rho\frac{v^2}{2} = \lambda\rho\frac{L_e}{D}\frac{v^2}{2} \quad (8)$$

where the first term represents the distributed pressure drops (depending on friction factor λ, on the fluid density ρ, on the length L and the diameter D of the channel, and on the fluid velocity v) and the second term represents the concentrated pressure drops (depending on the local pressure loss coefficient K_f, on the fluid density ρ and on the fluid velocity v). Their contribution can be combined in a single term by considering an equivalent circuit length L_e. The assumption of laminar flow field, for which $\lambda = 64/Re$ [49], coupled with the definition of volumetric flow $Q = vA$ (m^3/s) where A is a cross sectional flow area (m^2), leads to:

$$\Delta p = \lambda\rho\frac{L_e}{D}\frac{v^2}{2} = \frac{64\mu}{\rho vD}\rho\frac{L_e}{D}\frac{v^2}{2} = kQ \quad (9)$$

where the pressure drop (Δp) is a linear function of the volumetric flow rate (Q). Thus, assuming a reference value of pressure drops (Δp_{ref}) at nominal conditions, where the flow rate is Q_{ref}, the pressure drops obtained with different flow rates are computed as:

$$\Delta p = \Delta p_{ref} * \frac{Q}{Q_{ref}} \quad (10)$$

The values of Δp_{ref} and Q_{ref} are reported in Table 4.

Table 4 – Reference pressure drops and flow rates in FC channels.

	Δp_{ref} [bar]	Q_{ref} [m^3/h]
Anode channels	0.15	0.116
Cathode channels	0.15	0.515
Coolant channels	0.6	0.024

Table 5 – Blowers main features [50].

Compressor type	Max flow rate [m^3/h]	Engine power [kW]
COMP-A	9120	355
COMP-B	5480	200
COMP-C	3540	132

Air compression unit layout selection

Considering the required pressure increase and the nominal flow rates, air compression is based on the use of volumetric blowers. In particular, three models of rotary lobe compressors have been selected, able to treat different air flow rates, as detailed in Table 5. Based on contacts with manufacturers, it is

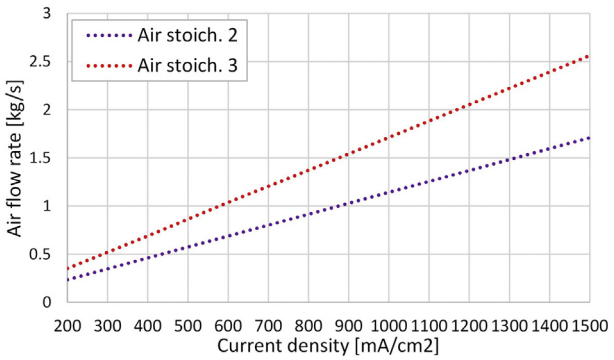

Fig. 5 – Air flow rates required by the fuel cell as a function of the load and the air stoichiometry.

assumed that the variable frequency-controlled motor allows, by changing the blower rotational speed, to decrease the air flow rate down to 15% of the maximum value. Calculation of the component performance is based on the blowers' efficiency curves.

Thus, considering the range of air flow rates required by the plant at different loads and air ratios to stoichiometry (see Fig. 5), three different compression solutions were compared in order to find the configuration that allows to supply air to the FC stacks while minimizing the power consumptions:

- one compressor COMP-A, able to process the maximum air flow required by the fuel cell;
- two compressors COMP-B, in parallel configuration;
- three compressors COMP-C, in parallel configuration.

The rotational speed at which each compressor (or couple/trio of identical compressors in parallel) have to work to provide a given air flow rate is shown in Fig. 6. The two graphs refer to fixed pressure gains equal to 0.8 bar and 0.2 bar respectively, that are the maximum and minimum pressure gains expected for air in the FC power plant. Minimum and maximum air flow rate required are also evidenced by vertical lines. The first solution (only one compressor COMP-A, blue line with circle markers) makes possible the operation at maximum load and maximum air stoichiometry both at high and low pressure. On the contrary, at low pressure and below ~480 mA/cm^2 it is not possible to have air stoichiometry equal to 2; while below ~350 mA/cm^2 the air stoichiometry cannot be lower than 3. Thus, bleeding of a fraction of air after compression would be required in order to control the air stoichiometry, limiting the plant efficiency. A single COMP-B compressor allows an air stoichiometry equal to 3 at low pressure and minimum load (200 mA/cm^2). A maximum air flow of 1.8 kg/s is provided at high pressure, that is not sufficient to work at maximum load (1500 mA/cm^2), neither with air stoichiometry equal to 2 nor 3. Hence, the installation of a second compressor COMP-B in parallel configuration is needed. With one compressor COMP-C it is possible to work at the minimum load and air stoichiometry equal to 2, without any air bleeding. However, two compressors of this type in parallel configuration are necessary to increase the current above ~1100 mA/cm^2 while keeping the air stoichiometry at 2, and three compressors are required for the plant to work at maximum load and air stoichiometry equal to 3.

The total power consumptions of the different analysed cases are shown in Fig. 7. It can be stated that there are no

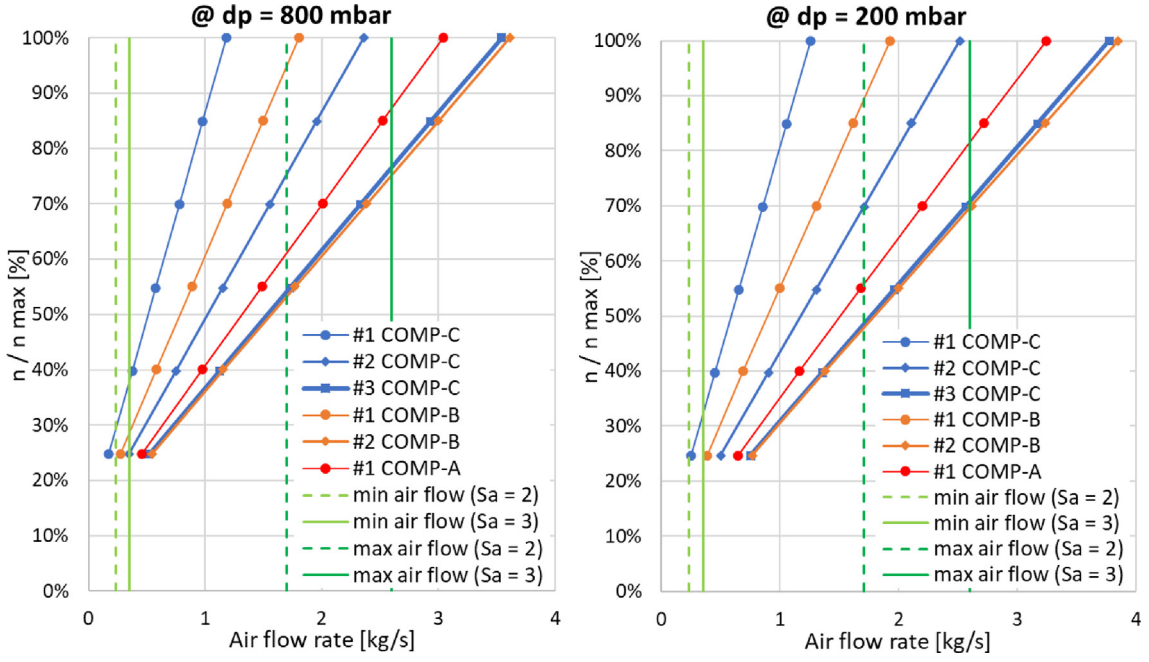

Fig. 6 – Air compressor rotational speed as a function of the air flow rate and compressor choice, with pressure gain 800 mbar (left side) and 200 mbar (right side).

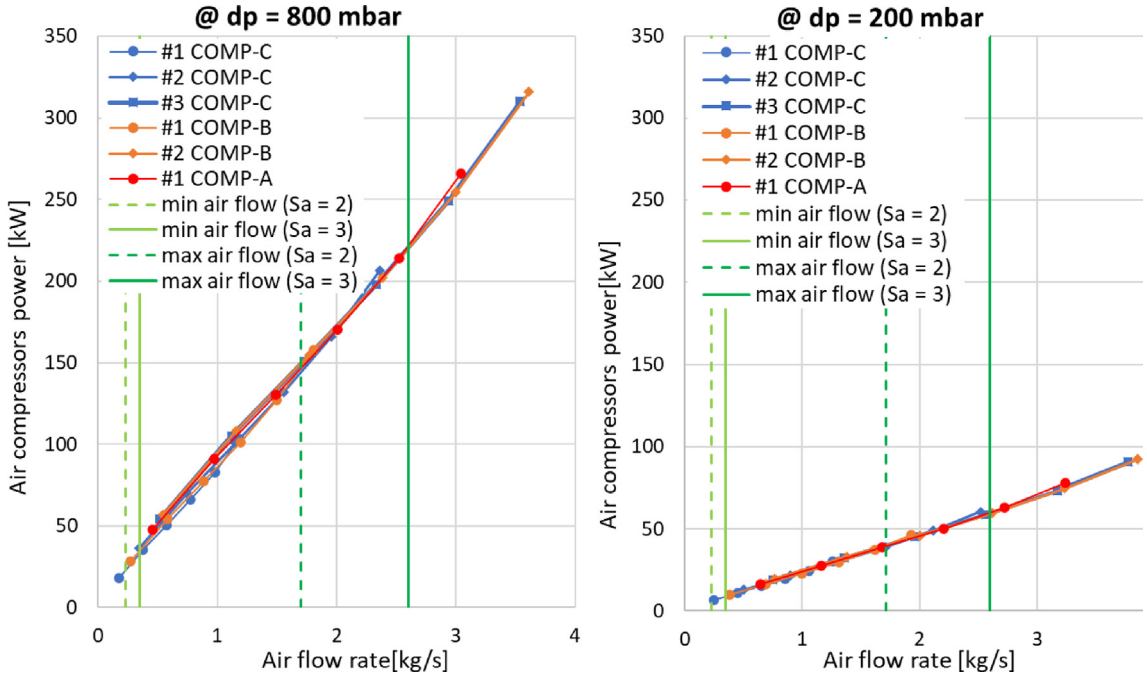

Fig. 7 – Power consumption of the air compressor as a function of the air flow rate, outlet pressure 800 mbar (left side) and 200 mbar (right side).

substantial changes in electrical consumption between the various cases. Therefore, the choice of the compressor should be carried out based on the possibility of controlling more accurately and effectively the plant as well as based on economic reasons. As it can be observed, the operating ranges of parallel units are overlapping, allowing in certain air flow ranges to operate the system with a different number of active machines (e.g. a single unit at high load or two units at low rotational speed) and frequent start-up or shutdown of the units can be avoided.

Simulations in the following chapters are carried out considering the intermediate solution, which represents a reasonable compromise: installation of two compressors COMP-B in parallel. It is assumed that only one compressor is activated at low current density and that the second compressor is switched on when the first one reaches the 80% of its maximum rotational speed, that is for an air flow rate of about 1.4 kg/s.

Balance of plant

The BoP components are all simulated through standard components available in the unit operation models library of Aspen Plus. BoP components are defined as a scale up of similar smaller components installed in the 100 kW Grasshopper pilot plant, whose technical specifications are known from the suppliers datasheets. Furthermore, the models of the BoP components are derived from models of similar components, previously developed and validated in the EU project DEMCOPEM [23,24].

The shower-type humidifiers that are adopted for both air and hydrogen humidification are composed by a water tank and a packed bed column. The water is pumped from the tank and sprayed at the top of the column, while the gas enters in the columns from its bottom. The gas flows through the column in counter-current direction with the water and leaves the column fully saturated. Liquid water drops entrained by the gas flow are removed with a demister before the gas leaves the packed-bed column. The humidification units are modelled using the adsorption column model (*RadFrac*) from Aspen Plus library. The column is discretized in 4 sections along the flow direction, for which vapour-liquid equilibrium is assumed. Constant values for the water recirculation flow rates and for pressure drops are assumed.

The two air compression units described in section 'Air compression unit layout selection' are simulated considering the isentropic compression model (*Compr*) from Aspen Plus library. Isentropic and mechanical efficiency are a function of the operating conditions (i.e. flow rate and pressure gain), so their values are here fixed interpolating on the compressor performance maps.

For hydrogen compression a liquid-ring compressor is installed. This kind of machine was chosen for its high reliability, already demonstrated in previous projects [23,50], despites its typical low efficiency. Moreover, it acts as a water separator and hydrogen saturator. A constant water flow has to be supplied to the compressor for maintaining stable the internal water ring and to cool down the system. A specific model for this component is not available, so the compressor electrical consumption is imposed from available data (5–65 kW, depending on hydrogen flow rate and pressure drops) and the temperature and phase conditions of the compressor outlet streams are obtained by solving an adiabatic phase equilibrium flash calculation on the feed streams (hydrogen and water).

The air expanders, installed only in the second case under investigation, are volumetric machines. Each of them is coupled with the compressor on a single shaft. They are

simulated with the expander component from Aspen Plus unit operation models library, as turbines with isentropic efficiency equal to 80% and mechanical efficiency equal to 90%.

The pumps for coolant fluid and humidifiers water circulation have isentropic efficiency of 70% and mechanical efficiency of 90%.

The heat exchangers are modelled in a countercurrent configuration. In order to consider the behavior of the system in variable conditions, the heat transfer area is calculated in design phase and then fixed. Empirical correlations are used to express the dependence of global heat transfer coefficients and pressure drops on the flow rates:

$$U = U_{nominal}\left(\frac{\dot{m}}{\dot{m}_{nominal}}\right)^{\frac{4}{5}} \tag{11}$$

$$\Delta p = k \cdot \dot{V}^2 \tag{12}$$

where the values of k are computed in order to have Δp_{nom} at $\dot{V}_{nom}$. The nominal values refer to the design conditions, as reported on the components' datasheets. The values of $U_{nominal}$, $\dot{m}_{nominal}$ and k are summarized in Table 6.

Pressure drops of the reactants in the circuits from the auxiliaries to the stacks and vice versa, as well as pressure drops of the coolant circuit, are calculated as function of the flow rate and circuit geometry using the *Pipe* model from Aspen Plus library.

Complete plant simulations results

The FCPP model is used to simulate the behavior of the FC power plant in different operating conditions, in order to identify the most efficient configuration and plant operating strategy. With the scope of offering ancillary services to the electric grid, the plant operates most of the time at partial load. Consequently, a wide range of currents is considered: from 20% to 150% of the nominal current value (which is 1 A/cm^2, so that the explored range is 0.2–1.5 A/cm^2).

In addition, the simulations aim to investigate the behavior of the plant while working in mildly pressurized conditions (up to 0.7 bar$_g$) and to assess the effectiveness of installing the air expander, in order to evidence in which conditions it may bring significant advantages.

The following constraints on the fuel cell operating conditions are imposed in all the simulation cases:

- air stoichiometry is kept constant at the nominal value by adjusting the air flow rate by varying the air compressors rotational speed.
- the hydrogen flow rate processed by the liquid ring compressor is limited in a narrow range, so the hydrogen stoichiometry changes with the load. This has a minor impact on cell performance as discussed in section 'PEMFC stack model'.
- the coolant flow rate is regulated by changing the pump rotational speed, aiming at limiting the temperature gain over the stack.
- the reactants temperature at air humidifier outlet is controlled to obtain an average 100% relative humidity for the air over the stack, while for the hydrogen the relative humidity at stack inlet is a constant value (50% related to 65 °C).
- Ambient temperature is assumed equal to 15 °C, however different values for the ambient temperature do not lead to significant changes in the results. Indeed, the heat generated in the stack is sufficient to keep the stack at the nominal temperature, even when ambient temperature decreases. Thus, only the coolant flow rate slightly changes.

Table 6 – Coefficients for heat transfer and pressure drops calculations in heat exchangers.

Heat exchanger	$U_{nominal}$ $\left[\frac{kW}{m^2K}\right]$	$\dot{m}_{nominal}$ $\left[\frac{kg}{s}\right]$	k $\left[\frac{bar}{m^3/s}\right]$
Coolant – external circuit	2.96	54.6	−47
Coolant – water for air humidifier	3.17	13.9	−197
Coolant – water for H_2 humidifier	6.2	15.1	−252

The first performance index is the gross efficiency, that considers the PEM fuel cell only (Eq. (13)). The second index is the net efficiency that represents the overall efficiency of the plants: electrical production is depurated from the DC/AC inverter losses (assuming the inverter efficiency $\eta_{inverter}$ equal to 95%) and from auxiliary power consumptions, including compressors and pumps consumptions. The energy input to the system is computed according to the Lower Heating Value (LHV) of the consumed hydrogen. Therefore, gross and net efficiency are expressed as:

$$\eta_{GROSS} = \frac{P_{FC}}{\dot{m}_{H_2} \cdot LHV} \tag{13}$$

$$\eta_{NET} = \frac{P_{FC} \cdot \eta_{inverter} - P_{auxiliaries}}{\dot{m}_{H_2} \cdot LHV} = \frac{P_{NET}}{\dot{m}_{H_2} \cdot LHV} \tag{14}$$

The gross power output and the corresponding gross efficiency are shown in Fig. 8. For any given gross power output, the gross efficiency increases by rising the backpressure and the highest gross efficiency is obtained with the highest

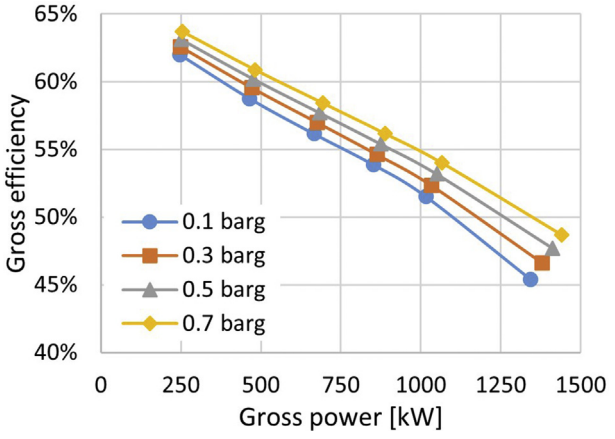

Fig. 8 – Gross efficiency Vs Gross power, for current densities ranging between 20% and 150% of the nominal value and for different levels of stack pressurization.

simulated value of backpressure (0.7 bar_g). Indeed, it is a direct consequence of the voltage increase given by the FC polarization curves analysed in section 'Modelling approach'. Therefore, by pressurizing the cells it is possible to obtain the same gross power with a lower current density and higher cell efficiency. At the same time, since the range of currents in which the cells operate is fixed (20%-150% of nominal current), with higher backpressure it is possible to generate slightly higher gross power. As shown in Fig. 8, the maximum generated gross power increases from 1343 kW to nearly 1441 kW moving from 0.1 bar_g to 0.7 bar_g.

Therefore, from the point of view of the fuel cell alone, pressurization appears to be always favourable. Anyway, pressurization involves changes also in the balance of plant consumption.

In the first case, where the expander is not installed, the auxiliary consumption is due to compressors and pumps only. The share of gross power that is consumed by the auxiliaries is shown in Fig. 9 for operation at nominal current, with minimum and maximum backpressure. The share of power consumption related to the compressors results always above 87% of the total auxiliary consumption. Similar results are obtained for different currents and at intermediate pressures.

In the second case, where the expander allows to recover energy from the cathode exhaust air, the total consumption is decreased by the expander power generation. The compressors power consumption and the expander power generation are shown as a function of the gross power, respectively in Figs. 10 and 11. As expected, both the air compressors consumption and the expanders generation increase by increasing the FC gross power (due to the increased air flow processed by the units) and by increasing the FC stacks backpressure (due to the increased pressure change). On the contrary, the hydrogen compressor works with a narrow range of volumetric flow rates, therefore its consumption variation is mainly determined by the variation in the pressure gain that it has to provide. This last parameter depends on the pressure drop in the hydrogen recirculation loop that is proportional to the volumetric flow rate. Therefore, the hydrogen compressor consumption increases by increasing the FC gross power (higher current density, hence higher hydrogen flow to the FC stacks) but decreases by increasing the FC stack backpressure (lower volumetric flow rate at higher pressures, for a given mass flow rate).

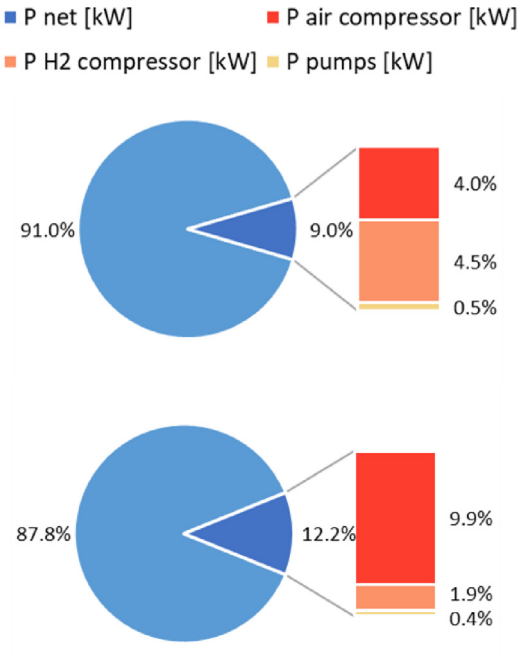

Fig. 9 – Share of auxiliary consumption on the gross power production, at nominal current density (i = 1 A/cm²) with cathode backpressure equal to 0.1 bar_g (above) and 0.7 bar_g (below). Case without expander.

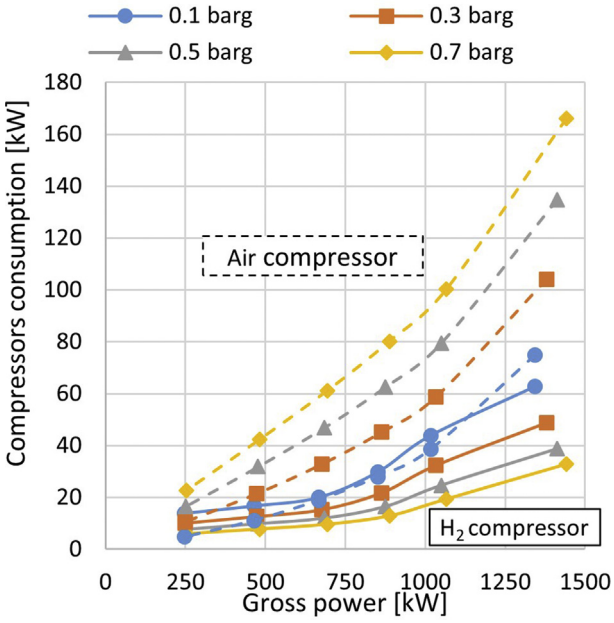

Fig. 10 – Air and hydrogen compressors power consumptions Vs gross power, for current density ranging between 20% and 150% of the nominal value and for different levels of stack pressurization.

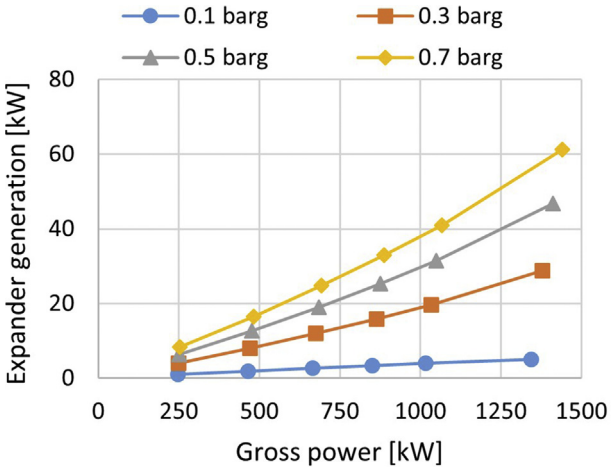

Fig. 11 – Air expander power generation Vs FC gross power, for current density ranging between 20% and 150% of the nominal value and for different levels of stack pressurization.

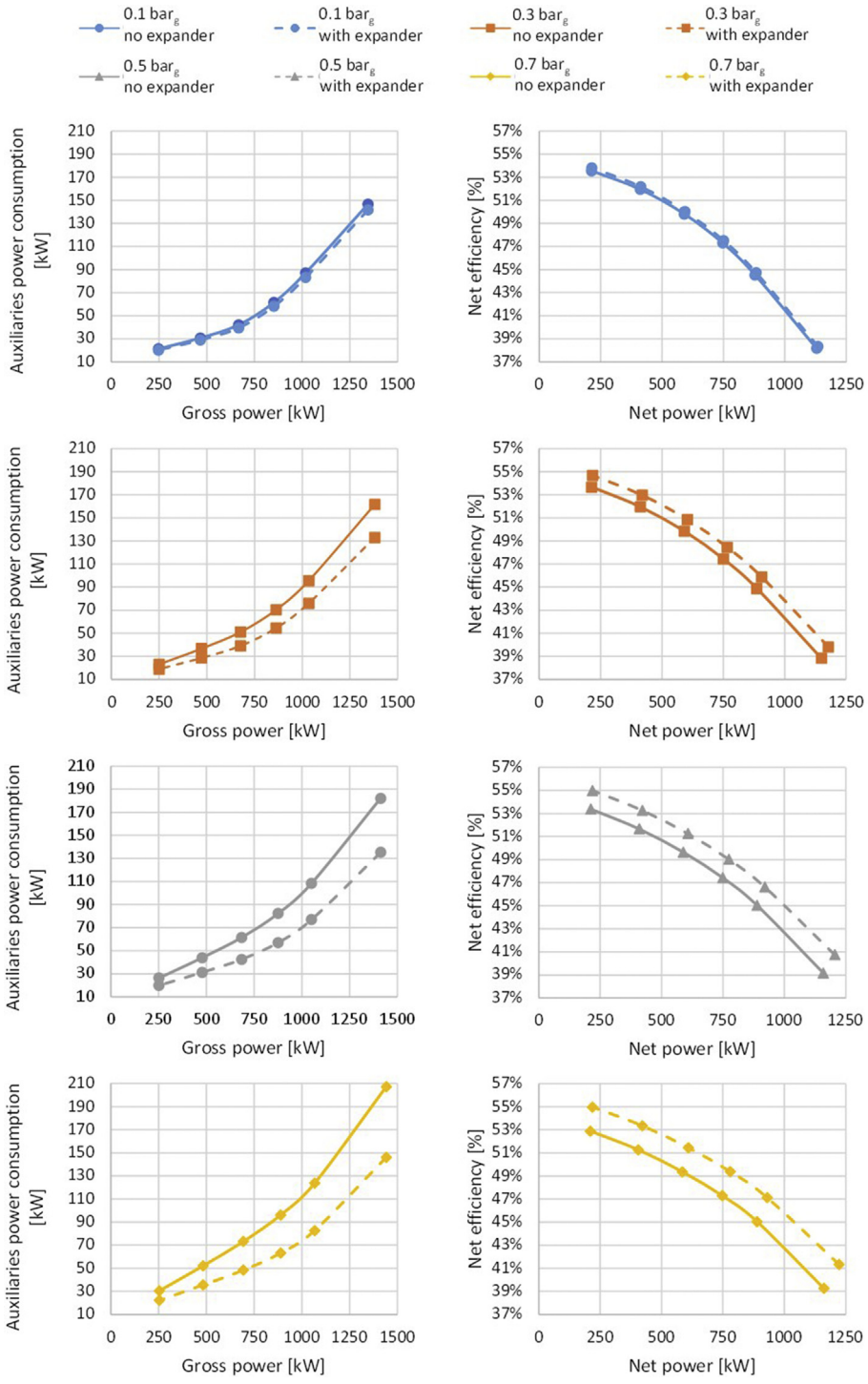

Fig. 12 – Auxiliary consumption vs gross power (left side column) and net efficiency vs net power (right side column), for current densities ranging between 20% and 150% of the nominal value, for different levels of stack pressurization, with and without an air expander for energy recovery.

The resulting total auxiliaries power consumption and the net efficiency of the plant are shown in Fig. 12 as a function of the FC gross and net power respectively.

For the cases without expander, a pressure gain always leads to higher power consumption from the auxiliaries, independently on the current density. Indeed, when the backpressure is increased, the air compression consumption rises faster than the drop in hydrogen compression consumption.

Without the expander, the net efficiency variation with the backpressure at a fixed net power depends on the net power itself. At low values of net power, the minimum net efficiency

Table 7 – Plant performances for increasing backpressure, with and without expander, at full and partial load.

p [bar_g]	i [A/cm^2]	P_{gross} [kW_{el}]	η_{gross} [$\%_{LHV}$]	Without expander		With expander	
				P_{net} [kW_{el}]	η_{net} [$\%_{LHV}$]	P_{net} [kW_{el}]	η_{net} [$\%_{LHV}$]
0.1	0.2	246.79	62.01	213.13	53.56	214.19	53.82
	0.6	666.06	56.16	590.73	49.81	593.40	50.03
	1	1016.89	51.51	878.93	44.53	882.93	44.73
0.3	0.2	249.13	62.60	213.56	53.66	217.59	54.68
	0.6	676.05	57.00	591.28	49.86	603.23	50.86
	1	1033.35	52.35	886.09	44.89	905.67	45.88
0.5	0.2	251.29	63.15	212.40	53.37	218.80	54.98
	0.6	684.41	57.71	588.70	49.64	607.73	51.24
	1	1049.80	53.18	888.92	45.03	920.41	46.63
0.7	0.2	253.58	63.72	210.46	52.89	218.78	54.97
	0.6	693.11	58.44	585.38	49.36	610.12	51.45
	1	1066.18	54.01	889.25	45.05	930.25	47.13

is obtained at the highest pressure (0.7 bar_g) while the maximum value is obtained at 0.3 bar_g. The situation changes for higher net power: above about 750 kW_{el} of net power generation, the highest net efficiency is obtained at 0.5 bar_g and the lowest at the minimum backpressure (0.1 bar_g). Finally, above about 880 kW_{el} net power, a further slightly increase in the net efficiency is obtained increasing the backpressure up to 0.7 bar_g. Therefore, the optimal operating strategy would consider to operate at 0.3 bar_g at minimum load, increasing then the stack backpressure up to 0.7 bar_g while increasing the load. The maximum net electric efficiency that the plant is able to reach by adopting this operation strategy is ~45%$_{LHV}$ at nominal current and up to ~54%$_{LHV}$ when the current decreases to its minimum value.

On the contrary, with the expander, the pressure that minimizes the auxiliary consumption is 0.3 bar_g and the one that maximizes the consumption is 0.7 bar_g.

When the expander is present, it becomes possible to reach both higher net power and higher net efficiency, especially in pressurized conditions. Indeed, at 0.1 bar_g the net efficiency gain brought about by the installation of the air expander is not appreciable due to the very low expander pressure ratio. At higher backpressure, the expander becomes more effective. The net efficiency gain with the introduction of the air expander is equal to 1%$_{pt}$ at 0.3 bar_g, 1.6%$_{pt}$ at 0.5 bar_g and 2.1%$_{pt}$ at 0.7 bar_g. Furthermore, when operating with the maximum current, at 0.7 bar_g a gain in the maximum net power of nearly 61 kW is obtained. Finally, the highest net efficiency is obtained at 0.7 bar_g for net loads above 600 kW_{el}, while for lower loads a slight increase (+0.01% at minimum load) in the net efficiency is obtained by reducing the backpressure to 0.5 bar_g. Thus, the plant can be practically operated at constant backpressure (0.7 bar_g), simplifying the control of the system without impacting on the system efficiency. Net efficiency up to ~47% $_{LHV}$ and ~55% $_{LHV}$ are reached for current density equal to the nominal and the minimum values, respectively.

Table 7 summarizes the values of net electric power generation and net electric efficiency, with and without the expander, for increasing stack backpressure and in correspondence to significant values of current density (representing the minimum load, the nominal load, and an intermediate load value). Hydrogen consumption varies between 133 Nm^3/h at minimum current and 662 Nm^3/h at nominal current.

Conclusions

A stationary model of the newly proposed MW-scale PEM fuel cell power plant, introduced as a possible scale up of the innovative flexible 100 kW pilot plant developed in the Grasshopper H2020 project, has been developed using the simulation tool Aspen Plus®. The plant model includes a custom model of the PEM FC stack, able to reproduce real cell performances through semi-empirical polarization curves, regressed on a current-voltage dataset obtained from previously unpublished experimental measurements on a test cell. Balance of plant components are simulated based on the standard library of components available in the software.

The model allows to simulate the plant behavior in different operating conditions and to compare different layout options. In this work, two layouts are compared, mainly differing for the presence of air expander units, recovering energy from the FC cathode exhaust air in order to drive the compressor units. Simulations are set up to analyze the plant performances for currents ranging from 20% to 150% of the nominal value, since the plant has to work at variable load to provide ancillary services to the electric grid.

Results show that increasing the pressure always allows to increase the FC stack gross efficiency. From the complete plant net efficiency point of view, also the auxiliary power consumption has to be considered. The consumption related to air and hydrogen compression is always above 87% of the total auxiliaries. Hydrogen compressor flow rate changes are limited, hence it consumes less at higher pressures and lower current density, where the volumetric flow rate is lower. On the contrary, air compressor consumption as well as air expander generation increase with increasing current density and backpressure, due to the increased flow rate and pressure change.

In the case without the expander, the highest net efficiency is obtained with a backpressure equal to 0.3 bar_g below 750

kW_{el} of net power generation, with a backpressure equal to 0.5 bar_g up to 880 kW_{el} and with 0.7 bar_g backpressure for higher values of net power. When the expander is present, it becomes possible to reach both a higher net power and a higher net efficiency, especially in pressurized conditions. The highest net efficiency is obtained with a backpressure equal to 0.7 bar_g above 600 kW_{el} of net power generation; while for a lower net power output the system efficiency slightly increases at 0.5 bar_g.

In conclusion, the installation of the expander allows to increase the net efficiency and run at higher pressures in all the operating range and, consequently, to reach a higher net power output with a given hydrogen consumption (the net electric efficiency is up to ~47%$_{LHV}$ at nominal current and up to ~55%$_{LHV}$ at minimum current). Furthermore, while without the expander the optimal operation strategy requires to change the stack backpressure while changing the load, with the expander it is possible to operate at constant pressure without a negative impact on the net efficiency.

Declaration of competing interest

The authors declare that they have no known competing financial interests or personal relationships that could have appeared to influence the work reported in this paper.

Acknowledgment

This project has received funding from the Fuel Cells and Hydrogen 2 Joint Undertaking under grant agreement No 779430. This Joint Undertaking receives support from the European Union's Horizon 2020 research and innovation programme, Hydrogen Europe and Hydrogen Europe research.

Nomenclature

BoP	Balance of Plant
FC	Fuel Cell
FCPP	Fuel Cell Power Plant
i	Current density [mA/cm^2]
LHV	Low Heating Value [kJ/kg]
$\dot{m}$	Mass flow rate [kg/s]
p	pressure [bar_g]
P	Power [kW]
PEM	Polymer Electrolyte Membrane
RH	Relative humidity [%]
S_a	Air stoichiometry [–]
V_{cell}	Cell voltage [mV]
x_{H_2O}	Water molar fraction [–]
x_{O_2}	Oxygen molar fraction [–]
x_{sat}	Water molar fraction at saturation [–]
η	Efficiency [%]

Subscripts

el	Electric
g	gauge
LHV	Low Heating Value

REFERENCES

[1] European Commission. A Clean Planet for all. A European long-term strategic vision for a prosperous, modern, competitive and climate neutral economy. COM 2018;773:114.
[2] European Commission. Clean energy for all Europeans. 2019.
[3] Doyle JR, Johlas H. Energy storage considerations for high renewable power penetration: a case study. In: SenGupta S, Zobaa A, Sherpa K, Bhoi A, editors. Advances in Smart Grid and Renewable Energy. Lecture Notes in Electrical Engineering, vol 435. Singapore: Springer; 2018. https://doi.org/10.1007/978-981-10-4286-7_40.
[4] Luo X, Wang J, Dooner M, Clarke J. Overview of current development in electrical energy storage technologies and the application potential in power system operation. Appl Energy 2015;137:511–36. https://doi.org/10.1016/j.apenergy.2014.09.081.
[5] Buttler A, Spliethо H. Current status of water electrolysis for energy storage , grid balancing and sector coupling via power-to-gas and power-to-liquids: a review. Renewable Sustain Energy Rev 2018;82(2017):2440–54. https://doi.org/10.1016/j.rser.2017.09.003.
[6] Amrouche SO, Rekioua D, Rekioua T, Bacha S. Overview of energy storage in renewable energy systems. Int J Hydrogen Energy 2016;41(45):20914–27. https://doi.org/10.1016/j.ijhydene.2016.06.243.
[7] Poullikkas A. A comparative overview of large-scale battery systems for electricity storage. Renew Sustain Energy Rev 2013;27:778–88. https://doi.org/10.1016/j.rser.2013.07.017.
[8] Paterakis NG, Erdinç O, Catalão JPS. An overview of Demand Response: key-elements and international experience. Renew Sustain Energy Rev 2017;69:871–91. https://doi.org/10.1016/j.rser.2016.11.167.
[9] Steinke F, Wolfrum P, Hoffmann C. Grid vs. storage in a 100% renewable Europe. Renew Energy 2013;50:826–32. https://doi.org/10.1016/j.renene.2012.07.044.
[10] JRC, European Union. Smart Grid projects in Europe: lessons learned and current developments. Publications Office of the EU 2011. https://doi.org/10.2790/32946.
[11] United Nations Economic Commission for Europe (UNECE), "Electricity system development: A focus on smart grids – overview of activities and players in smart grids.".
[12] Hossain MS, Madlool NA, Rahim NA, Selvaraj J, Pandey AK, Faheem A. "Role of smart grid in renewable energy: an overview. Renew Sustain Energy Rev 2016;60:1168–84. https://doi.org/10.1016/j.rser.2015.09.098.
[13] Novoa L, Neal R, Samuelsen S, Brouwer J. Fuel cell transmission integrated grid energy resources to support generation-constrained power systems. Appl Energy 2020;276:115485. https://doi.org/10.1016/j.apenergy.2020.115485.
[14] Lopes JAP, Hatziargyriou N, Mutale J, Djapic P, Jenkins N. Integrating distributed generation into electric power systems: a review of drivers, challenges and opportunities. Elec Power Syst Res 2007;77(9):1189–203. https://doi.org/10.1016/j.epsr.2006.08.016.
[15] IEA – International Energy Agency. Harnessing variable renewables – a guide to the balancing challenge. 2011. 612011171P1.
[16] Fuel Cells and Hydrogen Joint Undertaking (FCH JU). Multi – Annual Work Program 2014–2020. 2008.
[17] Entso-e. Electricity balancing in Europe – an overview of the European balancing market and electricity balancing guideline. 2018.

[18] COMMISSION REGULATION (EU) 2017/2195 of 23 November 2017 establishing a guideline on electricity balancing (Text with EEA relevance). Official Journal of the European Union, L 312 2017;60:6–53.
[19] Martin Beck MS. Overview of ancillary services. 2010. p. 1–6.
[20] Pirbazari AM. Ancillary services definitions, markets and practices in the world. In: 2010 IEEE/PES Transm. Distrib. Conf. Expo. Lat. Am. T D-LA 2010; 2011. p. 32–6. https://doi.org/10.1109/TDC-LA.2010.5762857.
[21] ACER – Agency for the Cooperation of Energy Regulators. Framework guidelines on system operation. 2011.
[22] "EU project Grasshopper." http://www.grasshopperproject.eu/ [accessed 06 June 2020].
[23] Campanari S, Guandalini G, Coolegem J, Ten Have J, Hayes P, Pichel AH. Modeling, development, and testing of a 2 MW polymeric Electrolyte membrane fuel cell plant fueled with hydrogen from a chlor-alkali industry. J Electrochem Energy Convers Storage 2019;16(4):1–9. https://doi.org/10.1115/1.4042923.
[24] Guandalini G, Foresti S, Campanari S, Coolegem J, ten Have J. Simulation of a 2 MW PEM fuel cell plant for hydrogen recovery from chlor-alkali industry. Energy Procedia 2017;105:1839–46. https://doi.org/10.1016/j.egypro.2017.03.538.
[25] Oh S, Kim K, Oh S, Kwak H. Optimal operation of a 1-kW PEMFC-based CHP system for residential applications. Appl Energy 2012;95:93–101. https://doi.org/10.1016/j.apenergy.2012.02.019.
[26] Tang Y, Yuan W, Pan M, Li Z, Chen G, Li Y. Experimental investigation of dynamic performance and transient responses of a kW-class PEM fuel cell stack under various load changes. Appl Energy 2010;87(4):1410–7. https://doi.org/10.1016/j.apenergy.2009.08.047.
[27] Verhage AJL, Coolegem JF, Mulder MJJ, Yildirim MH, De Bruijn FA. 30,000 h operation of a 70 kW stationary PEM fuel cell system using hydrogen from a chlorine factory. Int J Hydrogen Energy 2013;38(11):4714–24. https://doi.org/10.1016/j.ijhydene.2013.01.152.
[28] Karim H, Auvinen S, Ihonen J, Koski P, Pulkkinen V, Ker T. Operational experiences of PEMFC pilot plant using low grade hydrogen from sodium chlorate production process 2017;2. https://doi.org/10.1016/j.ijhydene.2017.09.056.
[29] Rivarolo M, Rattazzi D, Lamberti T, Magistri L. "Clean energy production by PEM fuel cells on tourist ships: a time-dependent analysis. Int J Hydrogen Energy 2020;45(47):25747–57. https://doi.org/10.1016/j.ijhydene.2019.12.086.
[30] Hoon C, et al. Development and demonstration of PEM fuel-cell-battery hybrid system for propulsion of tourist boat. Int J Hydrogen Energy 2015;41(5):3591–9. https://doi.org/10.1016/j.ijhydene.2015.12.186.
[31] Gharibeh HF, Yazdankhah AS, Azizian MR. Energy management of fuel cell electric vehicles based on working condition identification of energy storage systems , vehicle driving performance , and dynamic power factor. J Energy Storage 2020;31:101760. https://doi.org/10.1016/j.est.2020.101760.
[32] Hou J, Yang M. Control logics and strategies for air supply in PEM fuel cell engines. Appl Energy 2020;269:115059. https://doi.org/10.1016/j.apenergy.2020.115059.
[33] Zhang Y, Xu S, Lin C. Performance improvement of fuel cell systems based on turbine design and supercharging system matching. Appl Therm Eng 2020;180:115806. https://doi.org/10.1016/j.applthermaleng.2020.115806.
[34] Campanari S, Manzolini G, Beretti A, Wollrab U. Performance assessment of turbocharged PEM fuel cell systems for civil aircraft onboard power production. ASME J Eng Gas Turbines Power 2008;130(2). https://doi.org/10.1115/1.2772636. pp. 021701/1-7.
[35] Youssef ME, Al-nadi KE, Khalil MH. Lumped model for Proton Exchange Membrane Fuel Cell (PEMFC). Int J Electrochem Sci 2010;5:267–77.
[36] Mann RF, Amphlett JC, Hooper MAI, Jensen HM, Peppley BA, Roberge PR. Development and application of a generalised steady-state electrochemical model for a PEM fuel cell. J Power Sources 2000:173–80.
[37] Wang L, Husar A, Zhou T, Liu H. A parametric study of PEM fuel cell performances 2003;28:1263–72. https://doi.org/10.1016/S0360-3199(02)00284-7.
[38] Jeng KT, Lee SF, Tsai GF, Wang CH. Oxygen mass transfer in PEM fuel cell gas diffusion layers. J Power Sources 2004;138:41–50. https://doi.org/10.1016/j.jpowsour.2004.06.019.
[39] Lamanna JM, Kandlikar SG. Determination of effective water vapor diffusion coefficient in PEMFC gas diffusion layers. Int J Hydrogen Energy 2011:1–9. https://doi.org/10.1016/j.ijhydene.2011.01.036.
[40] Fly A, Thring RH. A comparison of evaporative and liquid cooling methods for fuel cell vehicles. Int J Hydrogen Energy 2016;41(32):14217–29. https://doi.org/10.1016/j.ijhydene.2016.06.089.
[41] Barelli L, Bidini G, Gallorini F, Ottaviano A. "An energetic – exergetic analysis of a residential CHP system based on PEM fuel cell. Appl Energy 2011;88(12):4334–42. https://doi.org/10.1016/j.apenergy.2011.04.059.
[42] Rabbani RA. Dynamic characteristics of an automotive fuel cell system for transitory load changes. Sustain Energy Technol Assess 2013. https://doi.org/10.1016/j.seta.2012.12.003.
[43] Rojas AC, et al. Control of the air supply subsystem in a PEMFC with balance of plant simulation. Sustainability 2017;1:1–23. https://doi.org/10.3390/su9010073.
[44] Malekbala MR, Khodadadi Azadboni R, Kazempoor P. Modeling and control OF a proton exchange membrane fuel cell with the air compressor according to. Therm Sci 2015;19(6):2065–78. https://doi.org/10.2298/TSCI130526071M.
[45] Barbir F, Gorgun H, Wang X. Relationship between pressure drop and cell resistance as a diagnostic tool for PEM fuel cells. J Power Sources 2005;141(1):96–101. https://doi.org/10.1016/j.jpowsour.2004.08.055.
[46] AspenTech software website. https://home.aspentech.com/ [accessed 06 June 2020].
[47] Baltic fuel cells GmbH webpage. https://www.balticfuelcells.de/qcfE.html [accessed 07 July 2020].
[48] Barbir F. PeM fuel cells: theory and practice. 2005.
[49] White Frank M. Fluid mechanics. 7th ed. 2009.
[50] AERZEN webpage. https://www.aerzen.com/it/prodotto/soffiatori-delta-blower-generation-5/performance.html.